


Spin-wave diffraction, caustic beam emission, and Talbot carpets in a yttrium iron garnet film with magnonic Fabry-Perot resonator gratings

Yifan Wang¹, Weizhi Yan¹, Nikolai Kuznetsov², Lukáš Flajšman², Huajun Qin^{1,3,*} and Sebastiaan van Dijken^{2,†}

¹*School of Physics and Technology, Wuhan University, Wuhan 430072, China*

²*Department of Applied Physics, Aalto University School of Science, FI-00076 Aalto, Finland*

³*Wuhan Institute of Quantum Technology, Wuhan 430206, China*

 (Received 18 April 2024; revised 6 June 2024; accepted 17 June 2024; published 16 July 2024)

We report spin-wave diffraction, caustic beam emission, and the formation of Talbot carpets in an yttrium iron garnet (YIG) film equipped with magnonic Fabry-Perot resonators. The resonator structures are created by patterning cobalt iron boron (Co-Fe-B) nanostripes on the YIG film. Small gaps in the Co-Fe-B nanostripes generate a magnetic field profile within the YIG film, functioning as a slit grating when the resonators block incoming spin waves at specific frequencies. We employ super-Nyquist sampling magneto-optical Kerr effect (SNS-MOKE) microscopy to image the transport of spin waves through the slits and supplement our experimental observations with micromagnetic simulations. For a single slit, we observe a transition from spin-wave diffraction to caustic beam emission as the slit size decreases. These phenomena are influenced by the effective magnetic field within the slit, which varies with the direction of magnetization in either the YIG film or the Co-Fe-B nanostripes. For multiple slits, we detect self-imaging of spin-wave profiles and the formation of Talbot carpets. Furthermore, we demonstrate active tuning of spin-wave interference patterns through magnetic switching in the Fabry-Perot resonators or by rotating the in-plane magnetization of the YIG film. The magnonic grating system described here integrates low-loss spin-wave transport and programmable spin-wave interference, offering potential applications in advanced magnonic computing devices.

DOI: [10.1103/PhysRevApplied.22.014038](https://doi.org/10.1103/PhysRevApplied.22.014038)

I. INTRODUCTION

Magnonics aims to utilize spin waves as information carriers in low-power logic circuits and unconventional computing devices [1–5]. Recently, a novel computing paradigm has emerged, based on programmable spin-wave interference in a magnetic film with multiple inputs and outputs [6–8]. This approach of utilizing an extended medium for spin-wave scattering, diffraction, and interference marks a departure from traditional magnonic circuits, where logic elements and interconnects are made of narrow waveguides [3]. Besides circumventing challenges inherent to signal processing in magnonic waveguides, such as their short spin-wave decay length, the need for large magnetic bias fields, or the guiding of spin waves through bends, the programming of wave interference patterns in magnetic films offers several attractive features for information processing. For example, wave interference in a magnonic scattering network can map input and output signals of a magnonic neural network with all-to-all

connectivity [7] or create magnonic components such as multiplexers, nonlinear switches, and circulators [6].

Interference patterns formed by wave diffraction on a grating of slits provide another avenue for configurable spin-wave computing. These patterns reproduce the spin-wave profile in the slits at specific distances behind the grating, a self-imaging phenomenon known as the Talbot effect. This effect has been observed in experiments on permalloy films [9] and simulated for exchange and magnetostatic spin waves in films with both perpendicular and in-plane magnetization [10]. Recently, programmable logic blocks utilizing the self-imaging effect with phase control at the inputs have been proposed [8]. Additionally, various diffraction gratings, including Rowland-type concave gratings [11,12] and Fresnel-zone plates [13], have been investigated for spectral analysis and the focusing of spin-wave signals.

Another effect that can be harnessed in magnonic devices with extended signal-processing areas is the emission of caustic beams. Caustic spin-wave beams, characterized by high intensity, a clearly defined propagation direction, and narrow angular width, can form in anisotropic magnetic media, such as films with in-plane

*Contact author: qinhuajun@whu.edu.cn

†Contact author: sebastiaan.van.dijken@aalto.fi

magnetization, when a pointlike source emits spin waves with a broad angular spectrum of wave vectors [14–20]. Due to their nondiffractive nature, caustic beams propagate over long distances and can be easily redirected by a magnetic boundary or local change of anisotropic dispersion [15,21]. Proof-of-principle caustic devices, such as spin-wave splitters [22] and frequency-division multiplexers [23] or demultiplexers [24], have already been proposed.

Studies on spin-wave diffraction, caustic beam emission, and spin-wave interference have utilized slits or gratings within magnetic films [9,12,13,20,25], as well as waveguides connected to an extended film [14,15,18,21]. In these implementations, the magnetic film is either patterned [9,14,15,18,20,21,25] or its properties are locally altered by focused ion-beam irradiation [12,13]. Here, we report on spin-wave diffraction, caustics, and the formation of Talbot carpets in a pristine yttrium iron garnet (YIG) film with in-plane magnetization. We investigate single- and multiple-slit structures using magnonic Fabry-Perot resonators [26,27] to locally block Damon-Eshbach spin waves at specific frequencies. The resonators are formed by patterning Co-Fe-B nanostructures on the YIG film. Gaps in the Co-Fe-B nanostructures create magnonic slits within the YIG film through which incoming spin waves can pass. This method of creating a magnonic grating maintains the

structural integrity and low magnetic damping of the YIG film, while enabling active control of spin-wave diffraction and interference patterns via independent magnetic switching in the YIG film and Co-Fe-B nanostructures.

II. RESULTS

A. Experimental configuration

The sample geometry and measurement configuration are illustrated in Fig. 1(a). The investigated sample comprises a 48-nm-thick YIG film with four parallel Co-Fe-B nanostructures patterned on top. The YIG film, with a Gilbert-damping constant of $(5.5 \pm 2) \times 10^{-4}$, has been grown on a (111)-oriented single-crystal $\text{Gd}_3\text{Ga}_5\text{O}_{12}$ (GGG) substrate by pulsed laser deposition (PLD) [28,29]. Co-Fe-B nanostructures, with a 40:40:20 composition, have been fabricated by electron-beam lithography, magnetron sputtering, and lift-off. The stripes are 240 nm wide, 24 nm thick, and have a center-to-center distance of 480 nm. The Co-Fe-B nanostructures and YIG film interact via dynamic dipolar fields across a 6-nm-thick TaO_x spacer. Together, they function as magnonic Fabry-Perot resonators [26, 27] that block propagating spin waves in the YIG film at specific frequencies. We have employed four parallel Co-Fe-B nanostructures to completely suppress spin-wave

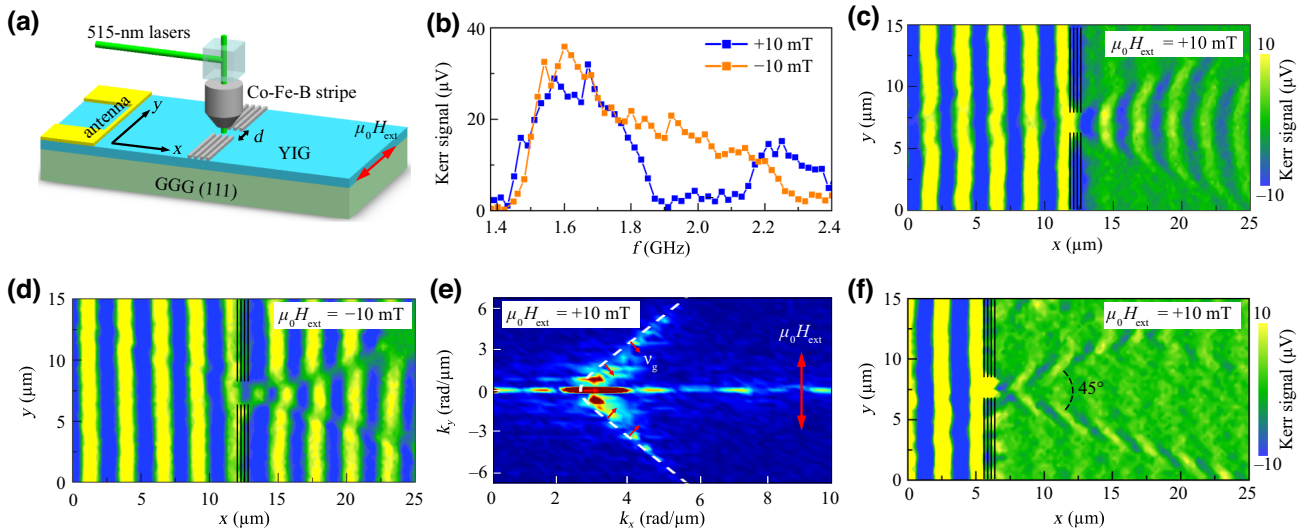


FIG. 1. (a) A schematic of the measurement geometry. The sample consists of a 48-nm-thick yttrium iron garnet (YIG) film with different magnonic slit structures (here, a single slit is shown). The slits are formed by patterning four Co-Fe-B nanostructures with small gaps on top of the YIG film. Together, the Co-Fe-B nanostructures and YIG film operate as magnonic Fabry-Perot resonators. Damon-Eshbach spin waves are excited by a $1\text{-}\mu\text{m}$ -wide microwave antenna and their transport through the slits is imaged by SNS-MOKE microscopy with a 515-nm femtosecond laser. (b) An SNS-MOKE frequency scan of the YIG film recorded behind four Co-Fe-B nanostructures at a magnetic bias field of $+10\text{ mT}$ and -10 mT along the y axis. (c),(d) An SNS-MOKE microscopy image of the spin-wave amplitude profile in the YIG film with a $2\text{-}\mu\text{m}$ -wide slit recorded at 2.1 GHz and a magnetic bias field of (c) $+10\text{ mT}$ and (d) -10 mT . (e) A fast-Fourier-transform (FFT) spectrum of the SNS-MOKE image in (c). The dashed line is the calculated isofrequency curve of the YIG film at 2.1 GHz and $+10\text{ mT}$. The small arrows indicate the direction of the spin-wave group velocity. (f) An SNS-MOKE microscopy image of caustic beam emission in the YIG film with a $1\text{-}\mu\text{m}$ -wide slit. The frequency is 2.1 GHz and the magnetic bias field is $+10\text{ mT}$. In all spin-wave maps, the black lines mark the position of the Co-Fe-B nanostructures.

transmission. The periodicity of the stripes has been chosen such that Bragg reflection does not occur within the frequency range of the experiments. Various slit structures and diffraction gratings have been created by introducing 1- μm -wide or 2- μm -wide gaps in the Co-Fe-B stripes. Spin waves have been excited in the YIG film by a 1- μm -wide microwave antenna with a Ta(3-nm)/Au(150-nm) structure, patterned 50 μm from the Fabry-Perot resonators by electron-beam lithography, evaporation, and lift-off. Wave diffraction on the slits, caustic beam emission, and spin-wave interference have been imaged using SNS-MOKE microscopy in a custom setup [26,30]. In most experiments, Damon-Eshbach spin waves have been excited by applying a magnetic bias field parallel to the microwave antenna.

B. Spin-wave diffraction and caustic beam formation by single-slit structures

In Fig. 1(b), we show an SNS-MOKE frequency scan of the YIG film with four Co-Fe-B nanostructures, recorded 10 μm behind the stripes in a magnetic bias field of +10 mT and -10 mT. A clear spin-wave transmission gap, ranging from approximately 1.8 GHz to 2.2 GHz, is observed at +10 mT. This gap results from the interaction between incoming and circulating spin waves in the YIG/Co-Fe-B Fabry-Perot resonators, as described in our previous works [26,27]. The wavelength of the spin waves within the resonators is smaller than in the uncovered YIG film and, because dynamic dipolar coupling between YIG and Co-Fe-B is chiral, it differs for opposite propagation directions. From micromagnetic simulations, we have derived wavelengths of 1.46 μm and 0.37 μm within the resonator at 2.1 GHz and +10 mT. For the field sweep direction used in the experiments, the magnetization of the YIG film and Co-Fe-B nanostructures align parallel at +10 mT and antiparallel at -10 mT. The spin-wave dispersion in the YIG/Co-Fe-B bilayer differs for these two magnetization states [26], leading to a transmission gap only at +10 mT. In the antiparallel configuration at -10 mT, the Co-Fe-B nanostructures minimally affect spin-wave propagation in the YIG film.

In Fig. 1(c), we show an SNS-MOKE microscopy image of the spin-wave amplitude profile in the YIG film with a 2- μm -wide slit, with the Co-Fe-B nanostructures indicated by black vertical lines. This measurement is performed at 2.1 GHz in a +10 mT field, a condition under which spin waves in YIG do not transmit across the Co-Fe-B nanostructures except at the slit area [see Fig. 1(b)]. For this parallel-magnetization state, the incoming Damon-Eshbach spin waves create a curved wave pattern behind the slit. In contrast, in a -10-mT field, the spin waves propagate across the four Co-Fe-B nanostructures without noticeable decay [Fig. 1(d)]. In the antiparallel-magnetization state, the YIG/Co-Fe-B Fabry-Perot resonators induce a

phase shift but do not significantly affect the amplitude or direction of the spin waves.

The curved wavefront in Fig. 1(c) results from spin-wave diffraction on the magnetically induced slit in the YIG film and caustic beam emission along the edges of the wave pattern. To illustrate this, we plot the fast Fourier transform (FFT) of the SNS-MOKE image in Fig. 1(e), along with the isofrequency curve of the YIG film at 2.1 GHz (dashed white line), calculated using the Kalinikos and Slavin model [31]. The high intensity at $(k_x, k_y) = (2.61, 0)$ rad/ μm in the FFT image corresponds to the wave vector of the incoming spin waves. The isofrequency curve is nonlinear for small k_y but linearizes rapidly at larger k_y . Consequently, spin waves with different wave vectors have the same group-velocity direction, as illustrated by the small red arrows in Fig. 1(e). While this is a prerequisite for caustic beam emission, the formation of such nondiffractive beams is effective only when the incoming spin waves scatter onto a pointlike source [14–20], i.e., when the slit size is considerably smaller than the wavelength. In the measurement shown in Fig. 1(c), the slit is 2 μm wide and the wavelength of incoming Damon-Eshbach spin waves is about 2.4 μm . Under this condition, the waves primarily diffract on the slit and only weak caustics are observed at the edges of the wave pattern. To enhance caustic beam formation, we have also investigated smaller slits. In Fig. 1(f), we show the spin-wave amplitude profile in the YIG film with a 1- μm -wide slit. In this case, two caustic beams are clearly defined, with their intensity remaining constant over a distance of 20 μm . The opening angle of the beams is approximately 45° , consistent with $2\tan^{-1}(\Delta k_x/\Delta k_y)$ in the linear part of the isofrequency curve.

To further investigate the characteristics of spin-wave diffraction and caustics, we have performed micromagnetic simulations using the MuMax3 software [32]. The simulation area has been set to $81.92 \times 40.96 \mu\text{m}^2$. The 48-nm-thick YIG film has been discretized into $40 \times 80 \times 6 \text{ nm}^3$ cells and periodic boundary conditions have been applied along the y axis. Four Co-Fe-B nanostructures, identical in dimensions to those used in the experiments, have been placed 6 nm above the YIG film. Spin waves have been excited in the YIG film by applying a 0.5-mT out-of-plane sinusoidal ac field over a 1- μm -wide region. A magnetic bias field of +10 mT or -10 mT has been applied along the y axis in most simulations. The input parameters for the simulations have been as follows: saturation magnetization $M_s = 192 \text{ kA/m}$ for YIG and $M_s = 1150 \text{ kA/m}$ for Co-Fe-B, exchange constant $A_{\text{ex}} = 3.1 \times 10^{-12} \text{ J/m}$ for YIG and $A_{\text{ex}} = 1.6 \times 10^{-11} \text{ J/m}$ for Co-Fe-B, and magnetic damping parameters $\alpha_{\text{YIG}} = 0.001$ and $\alpha_{\text{CoFeB}} = 0.005$. We have intentionally used a larger damping parameter for YIG than in the experiments to limit the computation time and reduce wave reflection from the edges of the simulation area. During continuous ac excitation,

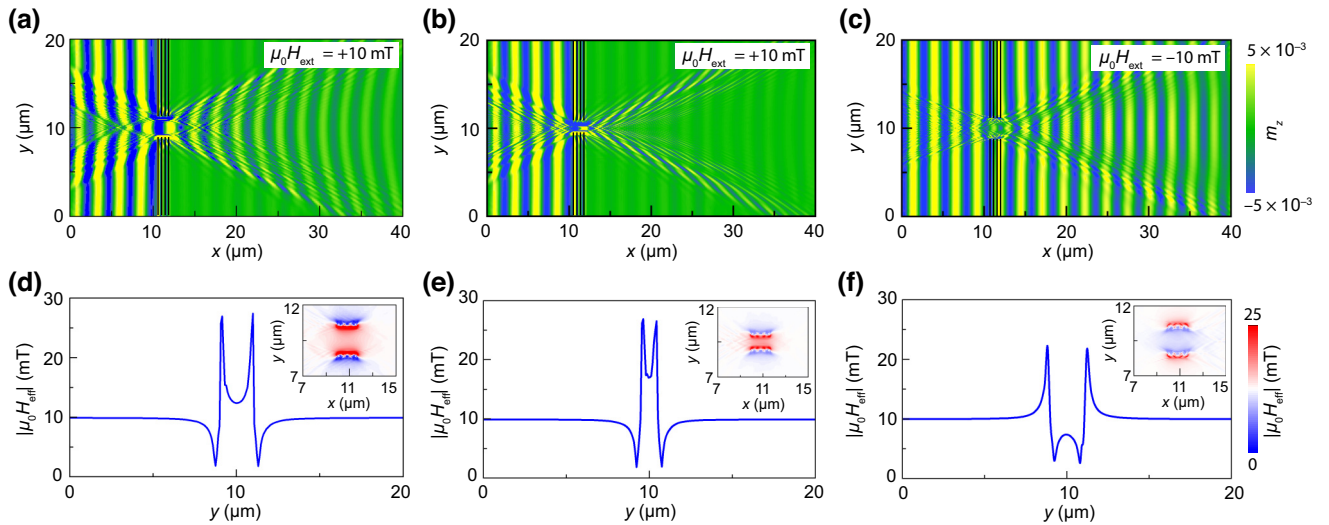


FIG. 2. (a),(b) Simulated spin-wave amplitude profiles in the YIG film with (a) a 2- μm -wide and (b) a 1- μm -wide slit. The excitation frequency is 2.1 GHz and the magnetic bias field is +10 mT (parallel-magnetization state). (c) The simulated spin-wave amplitude profile for a 2- μm -wide slit at 2.1 GHz and -10 mT (antiparallel-magnetization state). (d)–(f) Corresponding line profiles of the effective magnetic field across the magnetically induced slits in the YIG film. The plotted effective magnetic field is averaged over the YIG film thickness. The insets show the spatial distribution of the effective magnetic field in the slit area.

the time evolution of the z component (m_z) of the film magnetization has been recorded for 100 ns.

In Fig. 2(a), we present the simulated spin-wave amplitude profile for a 2- μm -wide slit at 2.1 GHz and +10 mT. The curved wavefront and the increased wave intensity at the pattern edges align well with the experimental data shown in Fig. 1(c), though the simulations reveal finer features not resolved by SNS-MOKE microscopy. Additionally, the micromagnetic simulations confirm the emission of caustic beams from a 1- μm -wide slit at +10 mT [Fig. 2(b)], as well as effective spin-wave transmission across the Co-Fe-B nanostripes with some wave diffraction and caustics at -10 mT [Fig. 2(c)]. In Figs. 2(d)–2(f), we illustrate the effective magnetic field in the YIG film for the simulation parameters corresponding to Figs. 2(a)–2(c). The magnetic stray field from the Co-Fe-B nanostripes determines the effective field profile of the slit in the YIG film. For the parallel-magnetization state at +10 mT [Figs. 2(d) and 2(e)], the effective magnetic field in the YIG film peaks near the edges of the Co-Fe-B nanostripes. In this configuration, the stray field from the Co-Fe-B nanostripes adds to the applied bias field, resulting in an effective magnetic field greater than +10 mT in the slit center, which increases as the slit size decreases. Consequently, the slit only becomes transparent to incoming spin waves above a threshold frequency. The 2.1 GHz used in Figs. 1 and 2 surpasses this threshold, allowing spin-wave transmission through the slit. Tailoring the effective field profile of magnetically induced slits enables programming of spin-wave diffraction patterns and caustic beams. For the antiparallel-magnetization state at -10 mT [Fig. 2(f)],

the effective magnetic field in the slit center is smaller than that in the YIG film. This local reduction in the effective field causes a wavelength down-conversion within the slit. Since the Fabry-Perot resonators with antiparallel magnetization do not block spin waves at 2.1 GHz, the diffracted spin waves and caustic beams emanating from the slit interfere with the incoming Damon-Eshbach spin waves behind the Co-Fe-B nanostripes, as depicted in Fig. 2(c).

C. Spin-wave interference and self-imaging in multiple-slit structures

To explore the formation of spin-wave diffraction patterns by multiple slits, we first focus on structures with two or three slits formed by four parallel Fabry-Perot resonators with 2- μm -wide gaps. In Fig. 3, we show SNS-MOKE measurements and micromagnetic simulations at an excitation frequency of 2.1 GHz and a magnetic bias field of +10 mT. In the double-slit structure, spin-wave interference results in the formation of an $n = 1$ self-image between the slits, as indicated by the dashed boxes in Figs. 3(a)–3(c). In wave physics, a self-image forms when all Fourier components present at a grating cross section reach an image line with a phase shift of 0° or 180° compared to the phase at the grating. Self-images on lines between the slits are formed by constructive interference of 180° -shifted waves. In our magnonic double-slit structure, this phase shift can clearly be seen in the phase-resolved SNS-MOKE image depicted in Fig. 3(c). The simulated effective magnetic field distribution in the YIG film with a

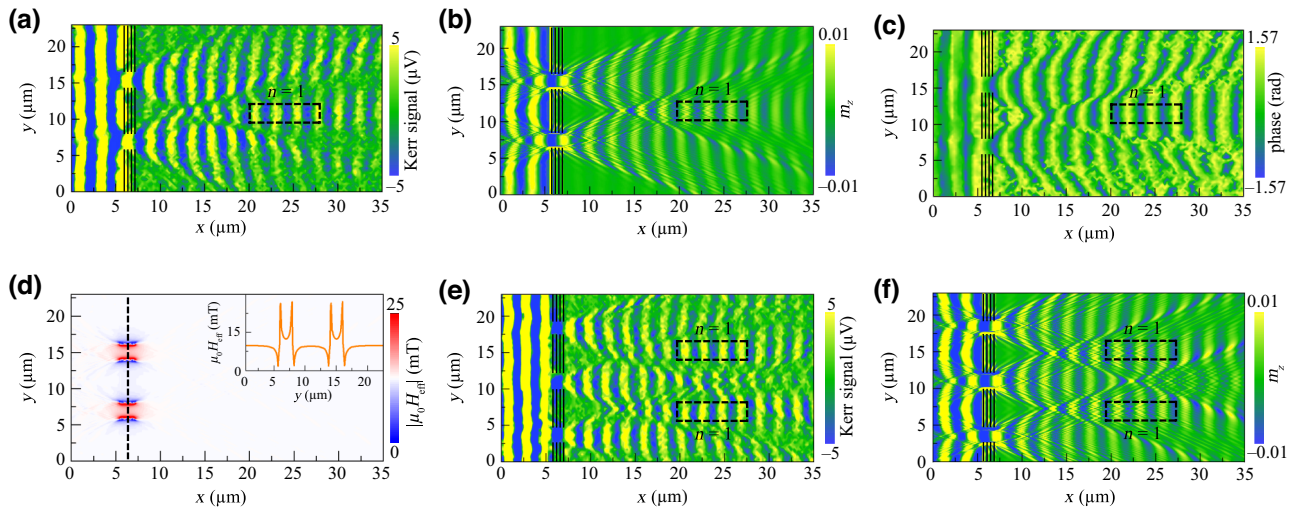


FIG. 3. (a),(b) The SNS-MOKE measurement and micromagnetic simulation of the spin-wave amplitude profile in the YIG film with a double-slit structure. The slits are $2\ \mu\text{m}$ wide, the excitation frequency is $2.1\ \text{GHz}$, and the magnetic bias field is $+10\ \text{mT}$. (c) An SNS-MOKE microscopy image of the spin-wave phase measured on the same structure and for the same experimental parameters as in (a). (d) The simulated spatial distribution of the effective magnetic field in the double-slit area of the YIG film. The inset shows a line profile of the effective magnetic field along the dashed line in the main graph. The applied magnetic field is $+10\ \text{mT}$. (e),(f) The SNS-MOKE measurement and micromagnetic simulation of the spin-wave amplitude profile in the YIG film with a triple-slit structure. The slits are $2\ \mu\text{m}$ wide, the excitation frequency is $2.1\ \text{GHz}$, and the magnetic bias field is $+10\ \text{mT}$. The period of the slit grating is $7.5\ \mu\text{m}$. In all spin-wave maps, the black lines mark the location of the Co-Fe-B nanostripes. The dashed boxes indicate the self-images with order number $n = 1$.

double slit is shown in Fig. 3(d). The nonuniform fields of the slits do not interact and thus the Fabry-Perot double-slit structure acts as two coherent spin-wave sources at $2.1\ \text{GHz}$.

Experimental and simulation data for a triple-slit structure are presented in Figs. 3(e) and 3(f). Adding another slit introduces an additional $n = 1$ self-image. Previously, spin-wave self-imaging has been observed in experiments on a permalloy film containing square-shaped holes [9]. Compared to that material system, the interference pattern in our YIG film with magnonic Fabry-Perot resonators decays much more slowly. In Fig. 3(e), the spin-wave amplitude measured at the slits and the $n = 1$ self-images are comparable, with the latter only about 5% smaller. This indicates that intense higher-order self-images can be obtained in this low-loss system, which is promising for the implementation of programmable logic blocks proposed recently [8].

Reversing the magnetic field to $-10\ \text{mT}$ significantly alters the interference pattern. In this antiparallel-magnetization configuration, the Fabry-Perot resonators no longer block incoming spin waves [see Fig. 1(d)]. Consequently, the wave pattern forming behind multiple slits results from the interference of plane waves, diffracted waves, and caustic beams.

We have further evaluated spin-wave interference in systems with larger gratings through micromagnetic simulations. In Fig. 4, we show simulation results for an infinite

Fabry-Perot resonator grating with $2\text{-}\mu\text{m}$ -wide slits. The YIG film thickness is $48\ \text{nm}$ and the grating period p is $5\ \mu\text{m}$. The spin-wave interference pattern behind the grating at $2.1\ \text{GHz}$ and $+10\ \text{mT}$ [Fig. 4(a)] resembles a Talbot carpet [8–10]. In this pattern, primary self-images with even-order numbers form on lines running through the grating slits, while secondary self-images with odd-order numbers appear on lines between the slits [10]. The envelope profiles of these self-images are similar, as shown by the spin-wave amplitude along $y = 12.5\ \mu\text{m}$ and $y = 15\ \mu\text{m}$ in Fig. 4(b). In isotropic media, such as in wave optics or forward-volume magnetostatic spin waves in magnonics, self-images of a diffraction grating appear at a specific distance $Z_T = np^2/\lambda$, known as the Talbot length. The spacing between self-images is therefore constant for a fixed wavelength (frequency) and grating period.

We have fast Fourier transformed the simulated interference pattern in Fig. 4(a) to analyze self-imaging in our YIG film with in-plane magnetization. The FFT result is plotted in Fig. 4(c) together with the calculated dispersion isofrequency curve at $2.1\ \text{GHz}$. We observe well-defined intensity maxima at $(k_x, k_y) = (2.61, 0)$, $(2.91, \pm 1.26)$, $(3.53, \pm 2.52)$, $(4.17, \pm 3.78)$ and $(4.79, \pm 5.06)$. The peak at $(k_x, k_y) = (2.61, 0)\ \text{rad}/\mu\text{m}$ corresponds to $\lambda = 2.4\ \mu\text{m}$ of the incoming spin waves. The other peaks represent the wave vectors of spin-wave modes contributing to the interference pattern. The k_y values are equally spaced by $\Delta k_y = 1.26\ \text{rad}/\mu\text{m}$, determined by the grating period

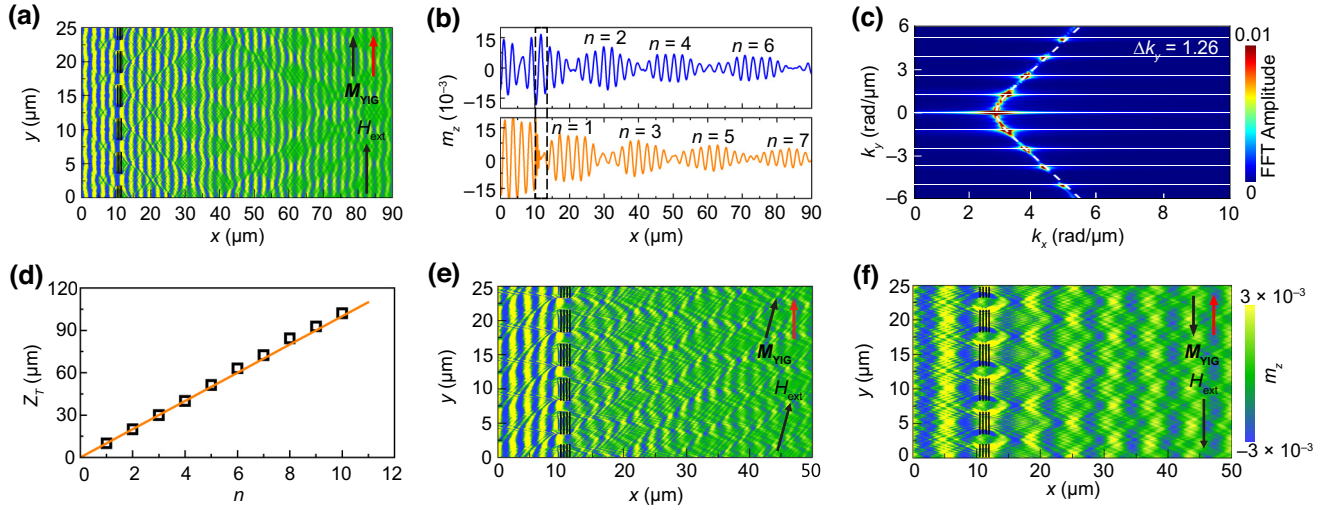


FIG. 4. (a) The simulated spin-wave amplitude profile for an infinite Fabry-Perot resonator grating with 2- μm -wide slits. The excitation frequency is 2.1 GHz, the magnetic bias field is +10 mT (parallel-magnetization state), and the grating period is 5 μm . (b) Line profiles of the spin-wave amplitude along $y = 12.5 \mu\text{m}$ (top) and $y = 15 \mu\text{m}$ (bottom) in (a). (c) The FFT spectrum of the spin-wave map in (a). The FFT spectrum of the grating and the dispersion isofrequency curve for 2.1 GHz are indicated by horizontal lines and a curved dashed line, respectively. (d) The distance of the spin-wave self-images from the grating extracted from the simulation in (a) (symbols), together with a calculation using $Z_T = np^2/\lambda$ (line). (e) The simulated spin-wave amplitude profile for the same grating as in (a) but with the 10-mT field applied at an angle of 15° with respect to the grating. The excitation frequency is 2.1 GHz. (f) The simulated spin-wave amplitude profile for the same grating as in (a) but for the antiparallel-magnetization state. The excitation frequency is 1.74 GHz and the magnetic bias field is -10 mT.

($\Delta k_y = 2\pi/p$). The k_x values result from the convolution of the Fourier spectrum of the grating [horizontal lines in Fig. 4(c)] with the dispersion isofrequency curve. Because the curve linearizes for small k_y , $\Delta k_x \approx \gamma \Delta k_y$, where γ is a constant. This translates to an approximately constant spacing between self-images along the x axis of $d \approx 2\pi/\Delta k_x \approx p/\gamma = p^2/\lambda$. Thus, the periodic repetition of spin-wave self-images in our YIG film with in-plane magnetization is well approximated by the Talbot length formula (Z_T) for isotropic media, as illustrated in Fig. 4(d).

Finally, we discuss tuning the spin-wave interference pattern by an external magnetic field. In our slit system, the magnetization alignment in the YIG film and Co-Fe-B nanostripes influences spin-wave diffraction and caustic beam emission due to the anisotropic spin-wave dispersion. The resulting interference pattern behind the slit grating therefore changes with magnetization rotation or reversal. For example, Fig. 4(e) shows the spin-wave amplitude profile for the same grating as in Fig. 4(a), but with the 10-mT bias field rotated by 15° . Here, the magnetization in YIG (black arrow) aligns along the magnetic bias field, while the magnetization of the Co-Fe-B nanostripes (red arrow) remains aligned with the long axis of the stripes due to shape anisotropy. This significantly alters the spin-wave interference pattern from the 0° field angle case [Fig. 4(a)]. Another example is the interference pattern for the antiparallel-magnetization state at 1.74 GHz and -10 mT shown in Fig. 4(f). In this configuration, incoming

spin waves are partially reflected by the magnonic Fabry-Perot resonators, resulting in a markedly different interference pattern compared to Fig. 4(a).

The approach for forming magnonic gratings in low-loss YIG films reported here is both scalable and programmable. Unlike methods that involve milling or etching holes into YIG films, which lack high spatial resolution, our method involves straightforward patterning of Co-Fe-B nanostripes. This technique preserves the structural integrity and spin-wave properties of YIG and allows for the creation of 1- μm -wide slits in YIG films with potential for further down-scaling. Since the Talbot length scales with the square of the grating period, magnonic computing concepts utilizing intense self-images require small slit sizes and grating periods. In addition to programmable spin-wave computing, our results can be applied to designing optics-inspired magnonic components, benefiting from strong nonreciprocity and nonlinearity. Potential applications include programmable spin-wave splitters, multiplexers, spectrometers, and focusing elements.

III. CONCLUSIONS

In summary, we have introduced a magnonic grating system using a continuous YIG film with magnonic Fabry-Perot resonators made of Co-Fe-B nanostripes. Small gaps

in these resonators create a magnetically induced slit grating in the YIG film at a frequency where the resonators block incoming spin waves. We have demonstrated a transition from spin-wave diffraction to caustic beam emission with decreasing slit size and shown that spin-wave interference behind a slit grating produces self-images at low bias fields. Due to the anisotropic spin-wave dispersion in the YIG film, diffraction, caustic beam emission, and the Talbot effect can be tuned by rotating the magnetization in the YIG film or Co-Fe-B nanostripes. Programming spin-wave interference patterns along with low-loss wave propagation in a YIG film with magnonic Fabry-Perot resonators will hopefully pave the way for implementing new computing concepts in magnonics.

The data that support the findings of this study are available from the corresponding authors upon reasonable request.

ACKNOWLEDGMENTS

This work was supported by the National Natural Science Foundation of China (Grant No. 12374119), the National Key Research and Development Program of China (Grant No. 2022YFA1402400), and the Academy of Finland (Grants No. 325480, No. 338748, and No. 13359125). Lithography was performed at the OtaNano-Micronova Nanofabrication Center, supported by Aalto University. We acknowledge the support from the Center for Nanoscience and Nanotechnology and the Supercomputing Center at Wuhan University.

H.J.Q. and S.v.D. led the project. Y.F.W., N.K., and L.F. performed the experiments. Y.F.W. and W.Z.Y. conducted the micromagnetic simulations. Y.F.W., H.J.Q., and S.v.D. wrote the manuscript. All authors discussed the results.

The authors declare no competing interests.

-
- [1] A. V. Chumak, V. I. Vasyuchka, A. A. Serga, and B. Hillebrands, Magnon spintronics, *Nat. Phys.* **11**, 453 (2015).
 - [2] G. Csaba, Á. Papp, and W. Porod, Perspectives of using spin waves for computing and signal processing, *Phys. Lett. A* **381**, 1471 (2017).
 - [3] A. Mahmoud, F. Ciubotaru, F. Vanderveken, A. V. Chumak, S. Hamdioui, C. Adelman, and S. Cotofana, Introduction to spin wave computing, *J. Appl. Phys.* **128**, 161101 (2020).
 - [4] A. Barman, G. Gubbiotti, S. Ladak, A. O. Adeyeye, M. Krawczyk, J. Gräfe, C. Adelman, S. Cotofana, A. Naeemi, V. I. Vasyuchka *et al.*, The 2021 magnonics roadmap, *J. Phys.: Condens. Matter* **33**, 413001 (2021).
 - [5] A. V. Chumak, P. Kabos, M. Wu, C. Abert, C. Adelman, A. O. Adeyeye, J. Akerman, F. G. Aliev, A. Anane, and A. Awad *et al.*, Advances in magnetism roadmap on spin-wave computing, *IEEE Trans. Magn.* **58**, 3149664 (2022).
 - [6] Q. Wang, A. V. Chumak, and P. Pirro, Inverse-design magnonic devices, *Nat. Commun.* **12**, 2636 (2021).
 - [7] Á. Papp, W. Porod, and G. Csaba, Nanoscale neural network using non-linear spin-wave interference, *Nat. Commun.* **12**, 6422 (2021).
 - [8] M. Gołębiewski, P. Gruszecki, and M. Krawczyk, Self-imaging based programmable spin-wave lookup tables, *Adv. Electron. Mater.* **8**, 2200373 (2022).
 - [9] S. Mansfeld, J. Topp, K. Martens, J. N. Toedt, W. Hansen, D. Heitmann, and S. Mendach, Spin wave diffraction and perfect imaging of a grating, *Phys. Rev. Lett.* **108**, 047204 (2012).
 - [10] M. Gołębiewski, P. Gruszecki, M. Krawczyk, and A. E. Serebryannikov, Spin-wave Talbot effect in a thin ferromagnetic film, *Phys. Rev. B* **102**, 134402 (2020).
 - [11] Á. Papp, W. Porod, Á. I. Csurgay, and G. Csaba, Nanoscale spectrum analyzer based on spin-wave interference, *Sci. Rep.* **7**, 9245 (2017).
 - [12] Á. Papp, M. Kiechle, S. Mendisch, V. Ahrens, L. Sahin, L. Seitner, W. Porod, G. Csaba, and M. Becherer, Experimental demonstration of a concave grating for spin waves in the Rowland arrangement, *Sci. Rep.* **11**, 14239 (2021).
 - [13] M. Kiechle, A. Papp, S. Mendisch, V. Ahrens, M. Golibrzuch, G. H. Bernstein, W. Porod, G. Csaba, and M. Becherer, Spin-wave optics in YIG realized by ion-beam irradiation, *Small* **19**, 2207293 (2023).
 - [14] V. E. Demidov, S. O. Demokritov, D. Birt, B. O’Gorman, M. Tsoi, and X. Li, Radiation of spin waves from the open end of a microscopic magnetic-film waveguide, *Phys. Rev. B* **80**, 014429 (2009).
 - [15] T. Schneider, A. A. Serga, A. V. Chumak, C. W. Sandweg, S. Trudel, S. Wolff, M. P. Kostylev, V. S. Tiberkevich, A. N. Slavin, and B. Hillebrands, Nondiffractive subwavelength wave beams in a medium with externally controlled anisotropy, *Phys. Rev. Lett.* **104**, 197203 (2010).
 - [16] R. Gieniusz, H. Ulrichs, V. D. Bessonov, U. Guzowska, A. I. Stognii, and A. Maziewski, Single antidot as a passive way to create caustic spin-wave beams in yttrium iron garnet films, *Appl. Phys. Lett.* **102**, 102409 (2013).
 - [17] C. S. Davies, A. V. Sadovnikov, S. V. Grishin, Y. P. Sharaevskii, S. A. Nikitov, and V. V. Kruglyak, Generation of propagating spin waves from regions of increased dynamic demagnetising field near magnetic antidots, *Appl. Phys. Lett.* **107**, 162401 (2015).
 - [18] Y. Shiota, S. Funada, R. Hisatomi, T. Moriyama, and T. Ono, Imaging of caustic-like spin wave beams using optical heterodyne detection, *Appl. Phys. Lett.* **116**, 192411 (2020).
 - [19] A. Wartelle, F. Vilsmeier, T. Taniguchi, and C. H. Back, Caustic spin wave beams in soft thin films: Properties and classification, *Phys. Rev. B* **107**, 144431 (2023).
 - [20] C. Riedel, T. Taniguchi, L. Körber, A. Kákay, and C. H. Back, Hybridization-induced spin-wave transmission stop band within a 1D diffraction grating, *Adv. Phys. Res.* **2**, 2200104 (2023).
 - [21] O. Dzyapko, I. V. Borisenko, V. E. Demidov, W. Pernice, and S. O. Demokritov, Reconfigurable heat-induced spin wave lenses, *Appl. Phys. Lett.* **109**, 232407 (2016).
 - [22] F. Heussner, A. A. Serga, T. Brächer, B. Hillebrands, and P. Pirro, A switchable spin-wave signal splitter for magnonic networks, *Appl. Phys. Lett.* **111**, 122401 (2017).

- [23] F. Heussner, M. Nabinger, T. Fischer, T. Brächer, A. A. Serga, B. Hillebrands, and P. Pirro, Frequency-division multiplexing in magnonic logic networks based on caustic-like spin-wave beams, *Phys. Status Solidi RRL* **12**, 1800409 (2018).
- [24] F. Heussner, G. Talmelli, M. Geilen, B. Heinz, T. Brächer, T. Meyer, F. Ciubotaru, C. Adelman, K. Yamamoto, A. A. Serga, B. Hillebrands, and P. Pirro, Experimental realization of a passive gigahertz frequency-division demultiplexer for magnonic logic networks, *Phys. Status Solidi RRL* **14**, 1900695 (2020).
- [25] U. Makartsou, M. Gołębiewski, U. Guzowska, A. Stognij, R. Gieniusz, and M. Krawczyk, Spin-wave self-imaging: Experimental and numerical demonstration of caustic and Talbot-like diffraction patterns, *Appl. Phys. Lett.* **124**, 192406 (2024).
- [26] H. Qin, R. B. Holländer, L. Flajšman, F. Hermann, R. Dreyer, G. Woltersdorf, and S. van Dijken, Nanoscale magnonic Fabry-Pérot resonator for low-loss spin-wave manipulation, *Nat. Commun.* **12**, 2293 (2021).
- [27] A. Talapatra, H. Qin, F. Schulz, L. Yao, L. Flajšman, M. Weigand, S. Wintz, and S. van Dijken, Imaging of short-wavelength spin waves in a nanometer-thick YIG/Co bilayer, *Appl. Phys. Lett.* **122**, 202404 (2023).
- [28] H. Qin, G.-J. Both, S. J. Hämäläinen, L. Yao, and S. van Dijken, Low-loss YIG-based magnonic crystals with large tunable bandgaps, *Nat. Commun.* **9**, 5445 (2018).
- [29] H. Qin, S. J. Hämäläinen, K. Arjas, J. Witteveen, and S. van Dijken, Propagating spin waves in nanometer-thick yttrium iron garnet films: Dependence on wave vector, magnetic field strength, and angle, *Phys. Rev. B* **98**, 224422 (2018).
- [30] R. Dreyer, N. Liebing, E. R. J. Edwards, A. Müller, and G. Woltersdorf, Spin-wave localization and guiding by magnon band structure engineering in yttrium iron garnet, *Phys. Rev. Mater.* **5**, 064411 (2021).
- [31] B. Kalinikos and A. Slavin, Theory of dipole-exchange spin wave spectrum for ferromagnetic films with mixed exchange boundary conditions, *J. Phys. C: Solid State Phys.* **19**, 7013 (1986).
- [32] A. Vansteenkiste, J. Leliaert, M. Dvornik, M. Helsen, F. Garcia-Sanchez, and B. Van Waeyenberge, The design and verification of MuMax3, *AIP Adv.* **4**, 107133 (2014).